

See discussions, stats, and author profiles for this publication at: <https://www.researchgate.net/publication/284244956>

Solar radiation as a global driver of hillslope asymmetry: Insights from an ecogeomorphic landscape evolution model

Article in *Water Resources Research* · November 2015

DOI: 10.1002/2015WR017103

CITATION

1

READS

110

3 authors, including:



Omer Yetemen

University of Newcastle

6 PUBLICATIONS 104 CITATIONS

SEE PROFILE



Erkan Istanbuluoglu

University of Washington Seattle

97 PUBLICATIONS 953 CITATIONS

SEE PROFILE



RESEARCH ARTICLE

10.1002/2015WR017103

Key Points:

- Spatial distribution of solar radiation controls hillslope asymmetry
- Channels develop on opposite hillslope aspects on two hemispheres
- Higher latitudes promote hillslope asymmetry

Correspondence to:

O. Yetemen,
omer.yetemen@usask.ca

Citation:

Yetemen, O., E. Istanbuluoglu, and A. R. Duvall (2015), Solar radiation as a global driver of hillslope asymmetry: Insights from an ecogeomorphic landscape evolution model, *Water Resour. Res.*, 51, 9843–9861, doi:10.1002/2015WR017103.

Received 14 FEB 2015

Accepted 16 NOV 2015

Accepted article online 14 NOV 2015

Published online 24 DEC 2015

Solar radiation as a global driver of hillslope asymmetry: Insights from an ecogeomorphic landscape evolution model

Omer Yetemen^{1,2}, Erkan Istanbuluoglu¹, and Alison R. Duvall³
¹Department of Civil and Environmental Engineering, University of Washington, Seattle, Washington, USA, ²Global Institute for Water Security, University of Saskatchewan, Saskatoon, Saskatchewan, Canada, ³Department of Earth and Space Sciences, University of Washington, Seattle, Washington, USA

Abstract Observations at the field, catchment, and continental scales across a range of arid and semiarid climates and latitudes reveal aspect-controlled patterns in soil properties, vegetation types, ecohydrologic fluxes, and hillslope morphology. Although the global distribution of solar radiation on earth's surface and its implications on vegetation dynamics are well documented, we know little about how variation of solar radiation across latitudes influence landscape evolution and resulting geomorphic difference. Here, we used a landscape evolution model that couples the continuity equations for water, sediment, and above-ground vegetation biomass at each model element in order to explore the controls of latitude and mean annual precipitation (MAP) on the development of hillslope asymmetry (HA). In our model, asymmetric hillslopes emerged from the competition between soil creep and vegetation-modulated fluvial transport, driven by spatial distribution of solar radiation. Latitude was a primary driver of HA because of its effects on the global distribution of solar radiation. In the Northern Hemisphere, north-facing slopes (NFS), which support more vegetation cover and have lower transport efficiency, get steeper toward the North Pole while south-facing slopes (SFS) get gentler. In the Southern Hemisphere, the patterns are reversed and SFS get steeper toward the South Pole. For any given latitude, MAP is found to have minor control on HA. Our results underscore the potential influence of solar radiation as a global control on the development of asymmetric hillslopes in fluvial landscapes.

1. Introduction

Hillslope-scale studies in soil-mantled semiarid ecosystems of the western U.S. consistently report steeper and more planar morphologies on north-facing slopes (NFS), and less steep, more concave, and highly dissected morphologies on south-facing slopes (SFS) [e.g., Walker, 1948; Melton, 1960; Carson and Kirkby, 1972; Branson and Shown, 1989]. The leading hypothesis that has found observational support relates these observations to sparser vegetation cover and greater rates of runoff erosion on SFS, and soil moisture storage, denser vegetation cover, and restrained fluvial activity on NFS, predominantly controlled by the ecohydrologic role of solar radiation and microclimate differences [Hadley, 1961; Carson and Kirkby, 1972; Branson and Shown, 1989; Istanbuluoglu et al., 2008; Yetemen et al., 2015].

A strong support to this hypothesis came from a field monitoring study that measured soil moisture, overland flow, and evapotranspiration on opposing NFS and SFS in central New Mexico, USA, where soil, vegetation, and hillslope morphologies present distinct aspect-controlled differences similar to those described above. The study revealed cooler, moister, and more densely vegetated NFS with greater evapotranspiration rates, and warmer and drier SFS with more frequent and larger runoff magnitudes [Gutiérrez-Jurado et al., 2013]. Growing research on this topic in other regions suggests that freeze-thaw [West et al., 2014], frost cracking [Anderson et al., 2013a], glacial processes [Naylor and Gabet, 2007], and weathering [Burnett et al., 2008] are among microclimate-driven processes that promote differential hillslope development.

Taking a continental perspective, Poulos et al. [2012] investigated hillslope asymmetry (HA) across the American Cordillera from 60°N to 60°S latitude. In this study, HA was described as log₁₀ of the ratio of median slopes of opposing aspects (N versus S, or E versus W) obtained from a 90 m DEM, using a 5 km by 5 km sliding window, and HA estimates were averaged for each latitude [Poulos et al., 2012]. Based on their observations, the N-to-S HA (HA_{N-S}), is nearly 0 at the equator, and systematically increases ($HA_{N-S} > 0$) in the

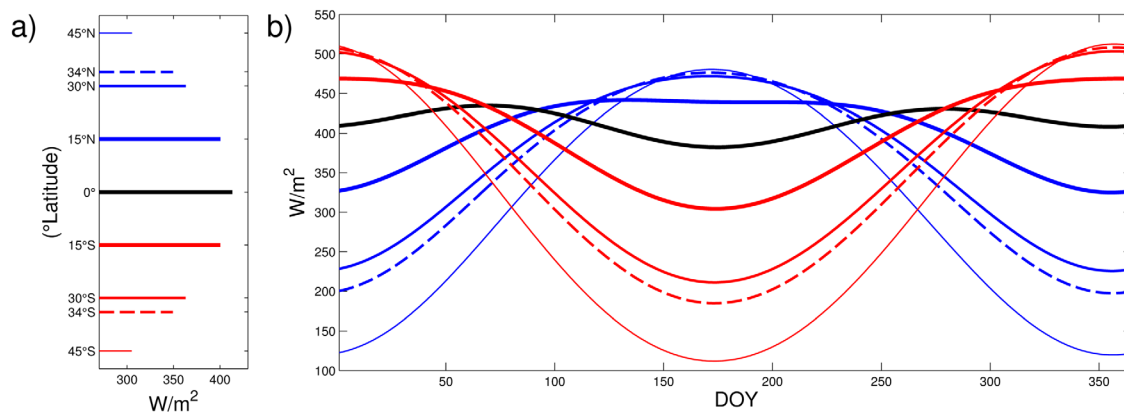


Figure 1. The role of latitude on extraterrestrial radiation: (a) annual, and (b) daily time scales. Annual insolation is maximum at the equator, and decreases with latitude toward North (N) and South (S). Seasonal amplitude of daily insolation grows with latitude, while the timing of peak insolation shifts from N to S. R_{ext} is estimated as a function of day of year (DOY), latitude, local slope, and aspect [Bras, 1990; Dingman, 2002].

Northern Hemisphere indicating steeper NFS, and decreases ($HA_{N-S} < 0$) in the Southern Hemisphere, indicating steeper SFS than their opposing counterparts. HA_{N-S} attains maximum absolute values at midlatitudes ($\sim 30^\circ$), and then begins to decrease in the Northern (increase in the Southern) Hemisphere, and finally changes signs above $\sim 49^\circ\text{N}$ (40°S) latitude. Their findings were consistent with Parsons [1988] who reported steeper NFS up to 45°N latitude and attributed this phenomenon to the role of microclimate differences on geomorphic processes at opposing aspects. Poulos *et al.* [2012] argued that the reversal in the HA_{N-S} at high latitudes may be due to the dominance of periglacial and glacial processes.

Coupling a solar radiation-driven ecohydrologic vegetation dynamics model with vegetation-modulated fluvial incision and transport equations in a model of landscape evolution, Yetemen *et al.* [2015] have demonstrated that in modeled catchments ($\sim 0.8 \text{ km}^2$) spatial and temporal characterization of solar radiation alone is sufficient to reproduce the first-order characteristics of observed aspect-related vegetation distributions, as well as hillslope and catchment-scale valley asymmetry in central New Mexico [Istanbulluoglu *et al.*, 2008; Yetemen *et al.*, 2010]. In their modeling experiments, microclimatic effects became more pronounced, leading to greater ecologic and geomorphic (ecogeomorphic) contrasts between opposing slopes as landscape relief increased as a result of higher rates of uplift used in the simulations, although hillslope diffusion was assumed spatially uniform.

Microclimatic causes driven by insolation have been suggested as a potential driver for differential hillslope development in low-to-midlatitudes [e.g., Parsons, 1988; Poulos *et al.*, 2012]. Figure 1 shows the role of latitude on extraterrestrial radiation, R_{ext} the amount of radiation on a horizontal surface on Earth would receive if there were no intervening atmosphere and clouds. Annual mean R_{ext} maximizes at the equator, and decreases toward the poles (Figure 1a). Seasonal variability in mean daily R_{ext} is minimal at the equator with a range of 380 and 430 W/m^2 . This variability increases with latitude approximately between 110 and 510 W/m^2 . A large number of environmental variables, such as local and regional climate (precipitation, temperature, wind speed), vegetation cover, lithology, and tectonic-climate feedbacks, may vary with latitude, influence a range of biotic and abiotic processes, and contribute to aspect-dependent ecosystem and landform development. Recent studies have begun to confirm these ideas by quantifying regolith production and transport on opposing hillslope aspects [Anderson *et al.*, 2013a; Ma *et al.*, 2013; West *et al.*, 2013, 2014]. However, we still do not know if latitude-dependent variations in the amount and spatial distribution of solar radiation alone (keeping all other environmental variables constant) can be sufficient to cause latitudinal patterns in hillslope asymmetry.

Motivated by the aforementioned model predictions of hillslope and valley asymmetry in central New Mexico by Yetemen *et al.* [2015], here we explore ecogeomorphic implications of latitude on landscape development by evolving landscapes from 45°N to 45°S latitudes using the Channel-Hillslope Integrated Landscape Development (CHILD) model for semiarid climate conditions. In order to only focus on latitude effects, we model the daily local amount and spatial distribution of insolation as a function of latitude, local slope, and aspect as described by Yetemen *et al.* [2015], while keeping precipitation seasonality and amount,

temperature, and turbulent evaporative forcing conditions identical in each latitude. Grass vegetation type is used in all simulations. Although this model setup is not realistic as regional climatology and vegetation cover naturally changes with latitude and glacial/periglacial processes could dictate erosion at high latitudes, neglecting such complexities allows us to isolate controls of solar radiation and a limited set of eco-geomorphic processes on hillslope asymmetry in a semiarid climate. As such, deviations of hillslope asymmetry (HA_{N-S}) calculated for actual landscapes compared to model predictions can be attributed to other local factors not considered in model experiments pursued in this paper.

Modeling experiments were used to address the following research questions: (1) can the observed relationship between HA_{N-S} and latitude [e.g., Poulos *et al.*, 2012] emerge as a result of differences in fluvial processes on opposing hillslopes mediated by differential development of vegetation? If so, (2) what is the sensitivity of vegetation productivity on hillslope aspect and latitude? (3) Does mean annual precipitation have any control on HA_{N-S} and latitude relationship? In this paper, we only consider vegetation impacts on fluvial detachment and transport because of the complexities and uncertainties in the ways of microclimatic controls on regolith thickness and creep transport. Hence, we only elucidate the influence of fluvial processes on hillslope asymmetry under spatially varying ecohydrologic conditions. First, we briefly describe the model theory and limitations, followed by the design of numerical experiments, then we present model simulations conducted for latitudes from 45°N to 45°S and discuss causalities between topographic evolution, insolation, and ecogeomorphic processes.

2. Model Theory

In this study, we used the CHILD landscape evolution model (LEM) [Tucker *et al.*, 2001], modified for distributed ecohydrologic simulations [e.g., Collins and Bras, 2010; Flores-Cervantes, 2010; Yetemen *et al.*, 2015]. The model couples the continuity equations for water, sediment, and aboveground vegetation biomass at each model element, and evolves fields of soil moisture, s , aboveground biomass, B (currently for grass vegetation type only), and elevation, Z , driven by stochastic rainfall, solar radiation, and landscape uplift. Implicit solar radiation and energy balance calculations were incorporated in the water balance model that resolve evapotranspiration. A coupled system of continuity equations is illustrated here with each equation in “generic” form. Fully developed forms of the continuity equations and details about solar radiation modeling can be found in Yetemen *et al.* [2015].

$$\text{Water : } nD_r \frac{\partial s}{\partial t} = I - \nabla \cdot \mathbf{q}_w - ET \{ ET_{\max} (T_{\max}^F, R_{\text{solar}}, LAI^*), s \} \quad (1)$$

$$\text{Biomass : } \frac{dB}{dt} = NPP(ET)\phi - k_B B \quad (2)$$

$$\text{Sediment : } \frac{\partial Z}{\partial t} = U - \nabla \cdot \mathbf{q}_{sd} - \nabla \cdot \mathbf{q}_{sf} [\tau_f(q_w, V_t)] \quad (3)$$

The water balance component in equation (1) tracks the changes in the amount of water within a soil depth of, D_r [L], with a maximum storage capacity of nD_r [L], where n is soil porosity, and s is the degree of saturation between 0 and 1 ($s = \theta/n$, θ : volumetric soil moisture content). Fluxes in the soil layer in a model element include the rate of infiltration, I [LT^{-1}] (constrained by the minimum of available water input, infiltration capacity, and available pore space in the root zone) [Collins and Bras, 2010]; divergence of water flux (sum of incoming overland and lateral subsurface flows minus outgoing flows divided by cell area), $\nabla \cdot \mathbf{q}_w$ [LT^{-1}]; and evapotranspiration, ET [LT^{-1}].

A piece-wise linear relationship is used to model ET as a function of s and ET_{\max} [LT^{-1}] (maximum rate of daily ET) at each model element. ET is at its upper limit ($ET = ET_{\max}$) when s is larger than a threshold, s^* . Below s^* , plants experience water stress, and ET reduces linearly as soil moisture dries between storms [Laio *et al.*, 2001]. In the model, solar radiation and its spatial distribution are incorporated in ET_{\max} . ET_{\max} is calculated as the weighted average of the rates of maximum transpiration, T_{\max} [LT^{-1}], and soil evaporation, E_s [LT^{-1}] (assumed proportional to T_{\max}), using LAI^* as the weighting coefficient: $ET_{\max} = T_{\max} LAI^* + (1 - LAI^*) E_s$, where LAI^* is the ratio of leaf area index [$\text{L}^2 \text{L}^{-2}$], LAI , of live vegetation cover to its ecologically limit value [e.g., Zhou *et al.*, 2013].

At each model element, T_{\max} is obtained by scaling the maximum transpiration rate of vegetation on flat surface, T_{\max}^f [LT^{-1}], by a solar radiation ratio, R_{solar} ($T_{\max} = T_{\max}^f \times R_{\text{solar}}$). T_{\max}^f is calculated by the Penman-Monteith equation using parameters for reference grass following Allen *et al.* [1998] on a flat and planar surface. R_{solar} can be conceptualized as the ratio of incoming shortwave radiation, R_s , on a hillslope element to that of a flat surface. This relationship is based on the assumption that radiation is the driver of transpiration in a semiarid region. Radiation received at the top of the atmosphere is extraterrestrial solar radiation, R_{ext} . R_{ext} can be calculated based on solar geometry as a function of topographic attributes (slope, aspect), latitude, and day of year (DOY) at each model cell [Bras, 1990]. Clear-sky radiation R_{cs} is the fraction of R_{ext} retained on the surface after the influence of atmospheric water vapor and dust is taken out, often using empirical relationships [Dingman, 2002]. R_s is the fraction of R_{cs} received by the surface further reduced by clouds and optical transmission losses. R_s can be empirically related to R_{ext} using the difference between the daily minimum and maximum temperatures [e.g., Hargreaves and Samani, 1982; Thornton and Running, 1999] or from the clear-sky radiation, R_{cs} , scaled with a function for cloud cover [Ivanov *et al.*, 2004]. In our model, considering spatially uniform cloud cover and atmospheric conditions (water vapor, dust), R_{solar} is estimated from the ratio of R_{cs} of a hillslope element to that of a flat surface, calculated at noon [see Yetemen *et al.*, 2015, Appendix A and B].

Grass vegetation type is modeled at each model element. Consistent with most process-based vegetation dynamics models, the rate of change in aboveground biomass, dB/dt ($\text{kgC m}^{-2} \text{d}^{-1}$), is a result of the balance between the net flux of carbon from the atmosphere to green plants (net primary productivity, NPP), and biomass loss due to plant senescence and disturbances. NPP ($\text{kgC/kgH}_2\text{O}$) is modeled as a function of ET following the water use efficiency concept [e.g., Williams and Albertson, 2005], and allocated to B (kgC m^{-2}) with a dynamic allocation coefficient, ϕ [$0 \leq \phi < 1$], that relates allocation inversely proportional to B . Plant senescence and drought-induced losses are represented by first-order decay equations [e.g., Montaldo *et al.*, 2005]. B is divided into live and dead biomass pools. Vegetation dynamics is coupled with water balance through ET (equations (1) and (2)). B regulates the amount of ET , through LAI , estimated from B [Yetemen *et al.*, 2015]. Floods are considered as a disturbance mechanism to vegetation following the model of Collins *et al.* [2004], which relates loss of grass cover linearly to excess shear stress. Implementation of this model in central New Mexico and parameter selection were discussed by Yetemen *et al.* [2015].

The continuity of sediment follows the Exner equation that describes the rate of change in elevation, Z , as a function of a sediment source term, (U) [LT^{-1}], and divergence of sediment flux per unit width by hillslope diffusion, $(\nabla \mathbf{q}_{\text{sd}})$ [LT^{-1}], and by fluvial transport, $(\nabla \mathbf{q}_{\text{sf}})$ [LT^{-1}] in a particular direction. Both local detachment and transport capacity equations are based on power functions of excess effective shear stress, τ_f ($\tau_{\text{eff}} - \tau_c$), where τ_c (Pa) is the critical shear stress for the initiation of detachment and transport. τ_{eff} is the shear stress that acts on sediment grains on the surface, and it is inversely related to total vegetation cover, V_t (live + dead biomass cover) [Istanbulluoglu and Bras, 2005]. V_t [$\text{m}^2 \text{m}^{-2}$] is calculated from modeled total LAI , LAI_t .

Sediment flux by hillslope diffusion is calculated based on the nonlinear hillslope diffusion model of Roering *et al.* [1999], and hillslope diffusivity is assumed spatially uniform [cf. Pierce and Colman, 1986]. There is evidence that a climate change-driven vegetation succession from grass and shrub species to forest vegetation enhances hillslope diffusion due to growing bioturbation [Roering *et al.*, 2004; Almond *et al.*, 2008; Hughes *et al.*, 2009]. Higher hillslope diffusion has been reported in humid forested basins undergoing bioturbation [Nash, 1980; Black and Montgomery, 1991; Roering *et al.*, 2002] than for arid and semiarid grass and shrubland ecosystems where physical disturbances such as rainsplash contribute to sediment production [Hanks, 2000; Martin, 2000; Gabet, 2003]. However, we are unaware of any research that have related hillslope diffusion to vegetation biomass or cover fraction across a monoculture region. As a single type of vegetation is modeled in this study, using a spatially uniform diffusivity constant is deemed appropriate. Besides vegetation, other environmental factors controlled by aspect-mediated microclimates can affect hillslope diffusion. For example, in forested watersheds in central Pennsylvania, USA, West *et al.* [2014] found twofold greater hillslope diffusivity on SFS than on NFS, and related this to a higher frequency of freeze-thaw cycles on SFS. Air and surface temperature-driven processes such as freeze-thaw are neglected in this study, as in this first implementation of the model across latitudes temperature is not explicitly modeled.

The model is driven by stochastic storms, with each storm pulse characterized by a depth, duration, and an interstorm duration using a modified rectangular-pulse Poisson-process method [e.g., Rodríguez-Iturbe and

Eagleson, 1987] with seasonally varying parameters. T_{\max}^F is first approximated by a sinusoidal function fitted to calculated reference grass transpiration using the Penman-Monteith model from meteorological station data. The sinusoidal function for T_{\max}^F is then used deterministically as a function of time in long-term simulations. A detailed description of the model, comparison of its ecohydrologic components against observations, and preliminary model experiments that examine the role of solar radiation on landscape development were presented for a field catchment in central New Mexico [Yetemen *et al.*, 2015].

3. Numerical Experiment Design

In this study, the CHILD LEM is run to explore the role of solar radiation on ecogeomorphic landscape evolution for representative semiarid conditions. The initial domain used identically in all simulations is a 900 m by 900 m east-facing sloping elevation field constructed of Voronoi polygons with 20 m node spacing and added random elevation perturbations with a mean of 2.5 m. Drainage is only permitted on the bottom of the sloping side of the domain. CHILD is run on this domain for a range of latitudes from 45°N to 45°S with 15° latitudinal increments for semiarid climatic conditions driven by a mean annual precipitation (MAP) from 200 mm to 500 mm and an uplift rate of 0.1 mm/yr. Fixed soil and grass vegetation parameters are used, selected for a field catchment in central New Mexico (34°N latitude) that produced model results consistent with ecohydrologic and geomorphic conditions in the field [Yetemen *et al.*, 2015]. For simplicity, change in vegetation functional type with climate is not allowed, as the semiarid climate used is consistent with grassland ecosystem ranges. A total of 56 simulations (two sets of simulations for the equator) are run for 800,000 years, a long enough duration to reach uplift-erosion equilibrium in the model. Details about the model setup and assumptions for latitudinal simulations are explained below.

3.1. Precipitation

CHILD is driven by MAP from 200 mm to 500 mm with 50 mm increments at each latitude. Climate is assumed to be stationary in each simulation. The annual mean value of T_{\max}^F is also varied consistent with MAP (see next section). The model is iterated for each generated actual storm, separated by an interstorm period during which the catchment dries through evapotranspiration driven by daily T_{\max}^F . Temporal and spatial variability of global climate, including glacial-interglacial or longer-term Milankovitch cycles, and latitudinal distribution of temperature and precipitation are neglected deliberately in order to focus on model sensitivity to solar radiation only.

In the simulations, seasonal rainfall characteristics are obtained from central New Mexico. This region receives approximately 250 mm of MAP, 50% of which falls during the North American Monsoon (NAM) between July and September [Vivoni *et al.*, 2008]. To simplify climate seasonality, we assumed distinct dry (9 month) and wet (3 month) seasons, each receiving 50% of MAP. In this region, solar peak and the wet season are in-phase with each other. When the model is implemented in the Southern Hemisphere, the location of the wet season is shifted to January–March period such that the solar peak and wet season are in-phase with each other, consistent with central New Mexico location (Figures 2c, 2d, wet season represented by a green band). More complex seasonal behavior including Mediterranean conditions (i.e., with out-of-phase solar peak and wet season) and more realistic latitudinal distribution of temperature and precipitation are not considered in this application of the model in order to focus on model response to solar radiation only.

Storm characteristics (intensity, duration, and interstorm duration) of the rectangular-pulse Poisson-process model in the LEM experiment are selected based on the MAP used in the simulation. For this purpose, we employed the rainfall climatology of the southwestern U.S., expressed empirically by relating observed storm parameters with MAP [Small, 2005; Istanbuloglu and Bras, 2006]. According to this literature, the mean annual interstorm duration, \bar{T}_b , decreases, and the number of storms (N_s) in a year increases with MAP (Figure 2a). In the model, \bar{T}_b is first selected for a given MAP, and it is further adjusted for wet and dry seasons with respect to the amount of rainfall in each season [Istanbuloglu and Bras, 2006]. Then, the mean inter storm duration, \bar{T}_r , is estimated based on N_s and \bar{T}_b and adjusted for seasonality [Small, 2005]. For both wet and dry seasons, empirical data suggest higher storm intensities as MAP grows (Figure 2b). Additionally, storms in the wet season are more intense than those in the dry season. To achieve reasonable runoff production consistent with semiarid climates, storm durations and intensities are adjusted using a scalar, while storm depth and number of storms in a year are preserved [Yetemen *et al.*, 2015]. The scalar used in this

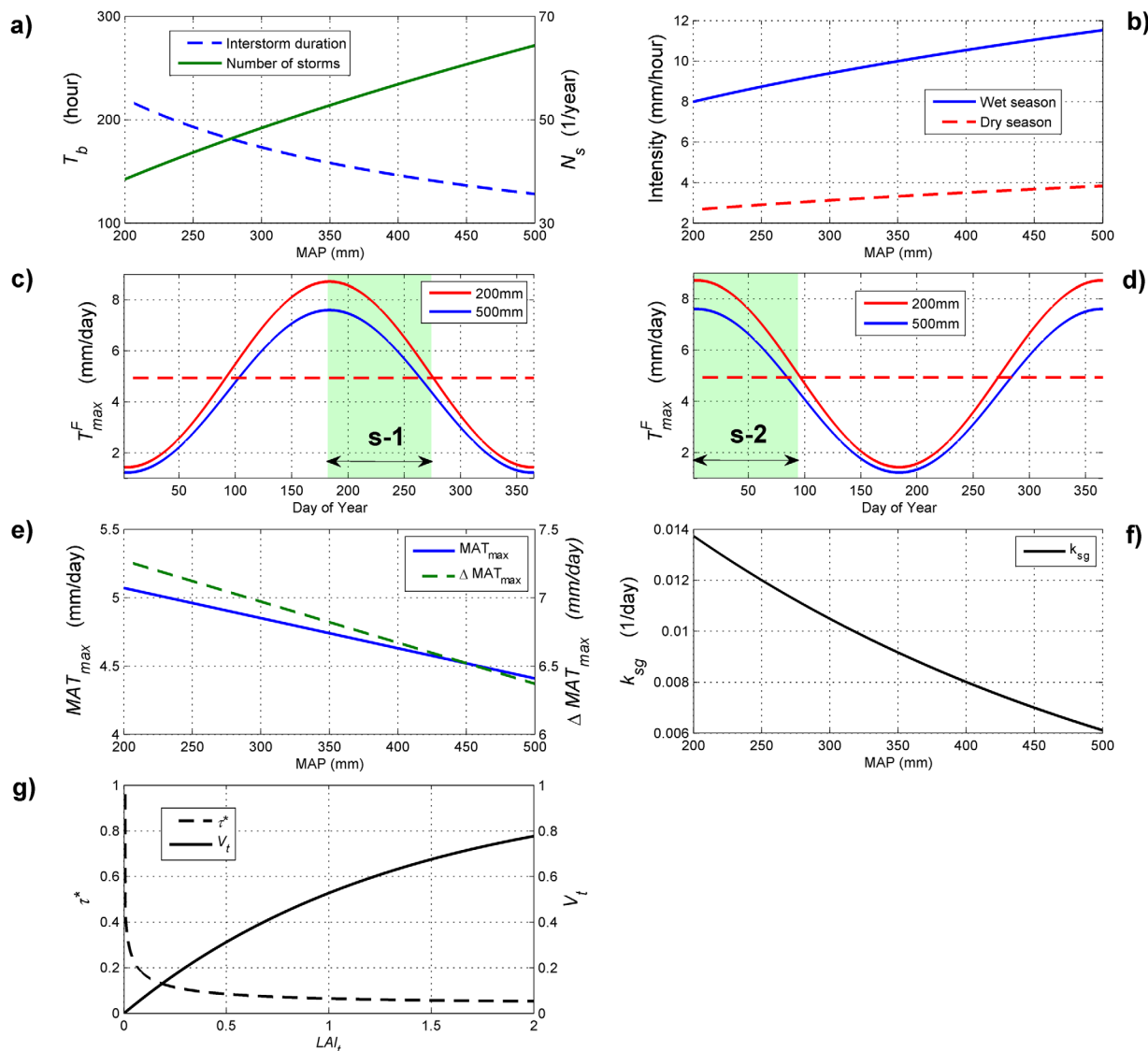


Figure 2. Illustration of several critical model assumptions: (a) Empirical relationships for the mean annual interstorm duration (\bar{T}_b) and annual number of storms (N_s) as a function of mean annual precipitation (MAP); (b) Mean storm intensity (mm/h) for wet and dry season precipitation as a function of MAP. A sixfold increase in intensities were used in the model to represent high-intensity and short-duration storms and generate realistic storm runoff magnitudes; Sinusoidal function used to represent the seasonal variability of T_{max}^F on a flat surface (T_{max}^F) as a function of DOY plotted for the wettest and driest MAP cases used in model runs for (c) the Northern Hemisphere and (d) the Southern Hemisphere, respectively. Green band highlight the timing of the wet season (July–September for the Northern Hemisphere (s-1) and January–March for the Southern Hemisphere (s-2)). T_{max}^F threshold used to start and end the growing season is represented with a red-dashed line; (e) Annual mean daily value of T_{max}^F (MAT_{max}) and the annual mean difference in minimum and maximum values of T_{max}^F (ΔMAT_{max}) used as parameters for the sinusoidal transpiration model in Figures 2c and 2d are predicted from MAP; (f) Empirical relationship that relates green biomass senescence coefficient to MAP; (g) Relationships of dimensionless shear stress τ^* and the total grass cover (V_t) on the total leaf area index LAI_t of the land surface.

paper amplifies observed rainfall intensity by a factor of 6, and reduces storm durations by the same factor. This method has been used in earlier modeling studies in semiarid climates that used the Poisson rectangular pulse method to ameliorate the known deficiencies of the model [e.g., Collins and Bras, 2010].

3.2. Maximum Transpiration, T_{max}^F

For long-term LEM simulations, seasonal changes in T_{max}^F for grass are represented using a sinusoidal function, calibrated for Penman-Monteith (P-M) estimated reference transpiration for central New Mexico (34°N latitude). The sinusoidal model for T_{max}^F has three parameters obtained from the daily P-M estimates: the annual mean daily value of T_{max}^F (MAT_{max}), the peak-to-trough amplitude of the sinusoidal function (ΔMAT_{max}), and the lag between peak solar forcing and peak of estimated T_{max}^F [Small, 2005]. One of challenges of this study was to develop a realistic T_{max}^F model for different latitudes. R_{ext} plotted for 34°N (34°S)

latitude peaks at DOY 172 (DOY 357) (Figure 1b). The peak and trough R_{ext} magnitudes for 34°N and 34°S latitudes only vary subtly. Based on central New Mexico data, T_{max}^F for 34°N, $T_{\text{max},34^\circ\text{N}}^F$, has a 10 day lag from the peak of R_{ext} at the same latitude, $R_{\text{ext},34^\circ\text{N}}$. In our long-term LEM experiment, to simplify evaporative forcing conditions we first neglected small differences in the peak and trough magnitudes of R_{ext} on 34°N and 34°S latitudes, and represent the sinusoidal model for T_{max}^F at the 34°S latitude, $T_{\text{max},34^\circ\text{S}}^F$, by shifting the location of the peak of the sinusoidal function for $T_{\text{max},34^\circ\text{N}}^F$ to DOY 2 (about 6 months). Figures 2c and 2d illustrate $T_{\text{max},34^\circ\text{N}}^F$ and $T_{\text{max},34^\circ\text{S}}^F$, respectively, which are then scaled by a ratio of R_{ext} at a given Northern Hemisphere (Southern Hemisphere) latitude, i , $R_{\text{ext},i^\circ\text{N}}$ ($R_{\text{ext},i^\circ\text{S}}$) to that at the 34°N (34°S) latitude as shown in equations (4a) and (4b). At the equator (4b) is used, as R_{ext} at the equator dips in the middle of the year consistent with $R_{\text{ext},34^\circ\text{S}}$.

$$T_{\text{max},i^\circ\text{N}}^F = T_{\text{max},34^\circ\text{N}}^F \frac{R_{\text{ext},i^\circ\text{N}}}{R_{\text{ext},34^\circ\text{N}}} \quad (4a)$$

$$T_{\text{max},i^\circ\text{S}}^F = T_{\text{max},34^\circ\text{S}}^F \frac{R_{\text{ext},i^\circ\text{S}}}{R_{\text{ext},34^\circ\text{S}}} \quad (4b)$$

To reflect the role of MAP on evapotranspiration, MAT_{max} and ΔMAT_{max} are related negatively with MAP (Figure 2e) based on data from New Mexico and Nebraska where grass is the dominant vegetation type [Istanbulluoglu et al., 2012]. This assumption is intuitive, due to the cooling effects of evapotranspiration in the lower atmosphere, greater relative humidity, and increased cloudiness as MAP grows [e.g., Cristea et al., 2013]. Daily variation of T_{max}^F in relation to MAP is demonstrated for 200 and 500 mm MAP for the 34°N and 34°S latitudes, respectively, in Figures 2c and 2d, where the horizontal line denotes a climatic growth threshold. When 30 day averaged T_{max}^F exceeds this threshold, the growing season starts.

The role of climate on the value of live biomass senescence coefficient (k_{sg}) is introduced to the model inversely proportional to MAP . This relationship was found to improve the model performance in regional grasslands across a MAP gradient in central Nebraska and used in New Mexico (Figure 2f) [Istanbulluoglu et al., 2012; Yetemen et al., 2015].

Incision and transport of sediment are driven by excess of effective shear stress, τ_f , in the model, which is inversely related to the total surface vegetation cover, V_t (live+dead biomass cover) [Istanbulluoglu and Bras, 2005]. V_t is calculated from modeled total LAI , LAI_t [Yetemen et al., 2015]. To illustrate how vegetation influences shear stress, we plot the ratio of τ_f to boundary shear stress, τ_b , (i.e., shear stress without vegetation influence) as a function of LAI_t , with soil and vegetation roughness values selected for the central New Mexico field site (Figure 2g). Vegetation on the ground increases the total roughness of the surface with respect to the grain roughness and decreases the shear stress that directly acts on soil grains. This model was tested using field observations from other literature [Istanbulluoglu and Bras, 2005]. According to the model, even a small amount of vegetation on the ground can reduce shear stress significantly.

The critical variable for this modeling study is R_{solar} used to calculate local rates of maximum transpiration from T_{max}^F , $T_{\text{max}} = T_{\text{max}}^F R_{\text{solar}}$. T_{max} is used as the boundary condition to the calculation of actual evapotranspiration in the model as part of water balance (equation (1)), and actual evapotranspiration is linearly used for the production of biomass. R_{solar} is estimated from the ratio of R_{cs} of a flat surface to that of a sloped surface, calculated at noon. We demonstrate how R_{solar} varies on NFS and SFS for 0° (the equator), 45°N, 30°N, 30°S and 45°S latitudes as a function of DOY and local slope (Figure 3). The horizontal double-headed arrow indicates the timing of the summer wet season from July to September termed as s-1 for the Northern Hemisphere. The horizontal double-headed arrow indicates the timing of the summer wet season from January to March termed as s-2 for the Southern Hemisphere. To examine the model sensitivity to the timing of the wet season at the equator, we used both cases.

Figure 3 illustrates the contrast in R_{solar} between NFS and SFS and how this contrast varies with latitude using end-member cases. When $R_{\text{solar}} > 1$, a sloped surface receives more radiation than flat surface, and when $R_{\text{solar}} < 1$, a sloped surface receives less radiation than flat surface. At the 45°N latitude, NFS consistently show lower R_{solar} than SFS for all topographic slopes throughout the year (Figures 3a and 3b). R_{solar} for NFS at the 45°N latitude is usually below 1, except for shallow slopes and during the peak of the solar forcing it can increase up to 1 (Figure 3a). On the other hand, R_{solar} for SFS is consistently above 1, except for very steep slopes and during the peak solar forcing it can go slightly below 1 (Figure 3b). In particular,

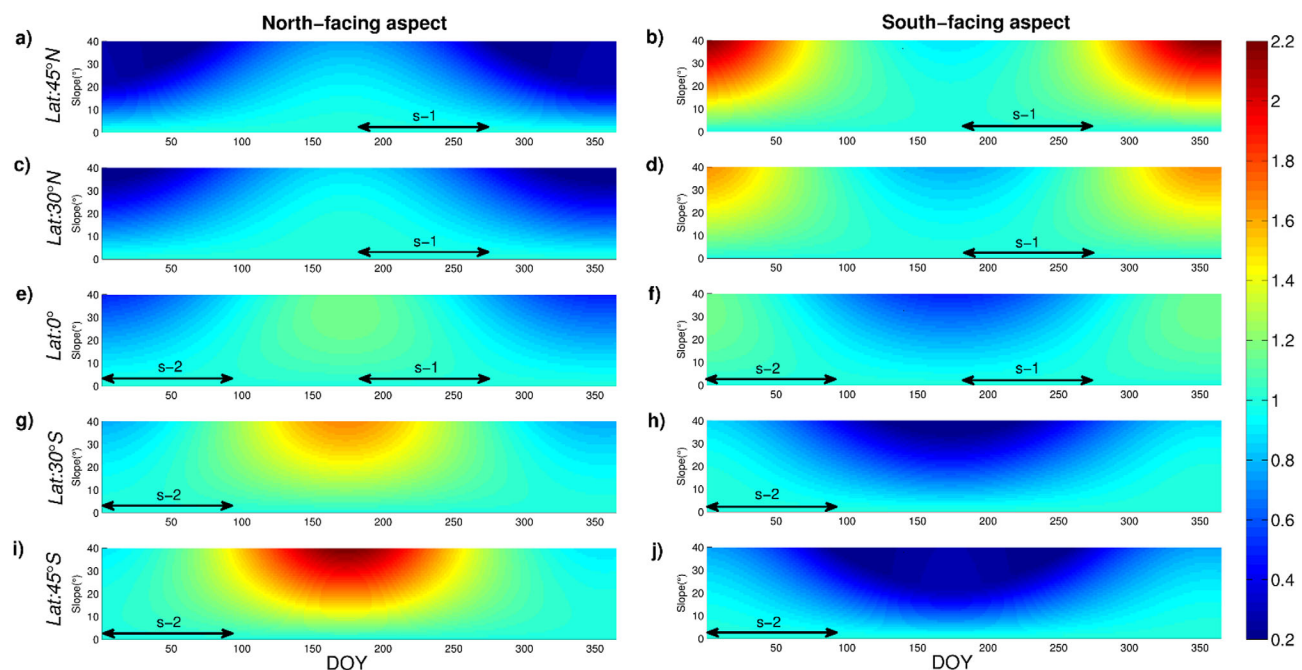


Figure 3. (top to bottom) Annual variation in R_{solar} (color bar at the bottom shows the scale) plotted as a function of local slope and day of year (DOY) for north-facing (a, c, e, g, i) and south-facing (b, d, f, h, j) aspects for 45°N, 30°N, 0°, 30°S, 45°S latitudes, respectively. Horizontal double-headed arrow indicates the wet season (half of the annual precipitation) used in the model. There are two sets of simulations for the equator case simulated with two different wet-season timing periods. The s-1 represents the wet season timing of the northern hemisphere, and s-2 represents the wet season timing of the southern hemisphere.

during the fall and winter seasons, the contrast in R_{solar} between NFS and SFS grows significantly for slopes steeper than 10°, where SFS can receive as much as eight times greater solar radiation than NFS. In the summer of the Northern Hemisphere, R_{solar} contrast between NFS and SFS drops.

At the 45°S latitude, the plotted R_{solar} fields for NFS and SFS are the same images of those for SFS and NFS, respectively, at the 45°N, with a half-year time lag as a result of the shift of the solar peak from June (DOY = 172) to December (DOY = 357) in the Southern Hemisphere (Figures 3i and 3j). Seasonally, similar to the Northern Hemisphere, R_{solar} contrast is higher during the winter and fall months, which is centered in the middle of the year, during which NFS can receive up to eight times greater solar radiation than SFS. R_{solar} contrast drops in the Southern Hemisphere during the spring and summer seasons of the Southern Hemisphere especially for gentle slopes (Figures 3i and 3j).

In the Northern Hemisphere approaching to the equator, the values of R_{solar} on SFS lose strength on all topographic gradients, while radiation on NFS grows (Figures 3e and 3f). NFS at the equator receive more radiation during the summer than SFS, while SFS receive more radiation during spring, winter, and fall. Even at the equator, the spatial distribution of R_{solar} throughout the year is not uniform, although the contrast is minimal compared to southern and northern latitudes. Beside these latitudes, we also plot the R_{solar} fields for 30°N and 30°S latitudes to show the transitions in the R_{solar} from the equator to high latitude (Figures 3c–3f). R_{solar} values at 30°N and 30°S latitudes show roughly similar patterns that are observed at 45°N and 45°S latitudes. However, the R_{solar} contrasts at 30°N and 30°S latitudes are lower than those at the 45°N and 45°S latitudes. And the period that R_{solar} contrast diminishes gets longer.

4. Results and Discussions

4.1. Modeled Landscape Morphology and Hillslope Asymmetry Across Latitudes

Figure 4 presents upslope contributing area maps of sample modeled drainage basins for 45°N, 0° (s-1 wet season), and 45°S latitudes, driven by 200, 350, and 500 mm of MAP. Darker colors represent the channel network. North-to-south hillslope asymmetry indices (HA_{N-S}) calculated for each domain using the method of Poulos et al. [2012] are given in the figure. Model results show clear evidence of latitudinal control on channel network development. In the Northern Hemisphere (45°N latitude), channels preferentially develop

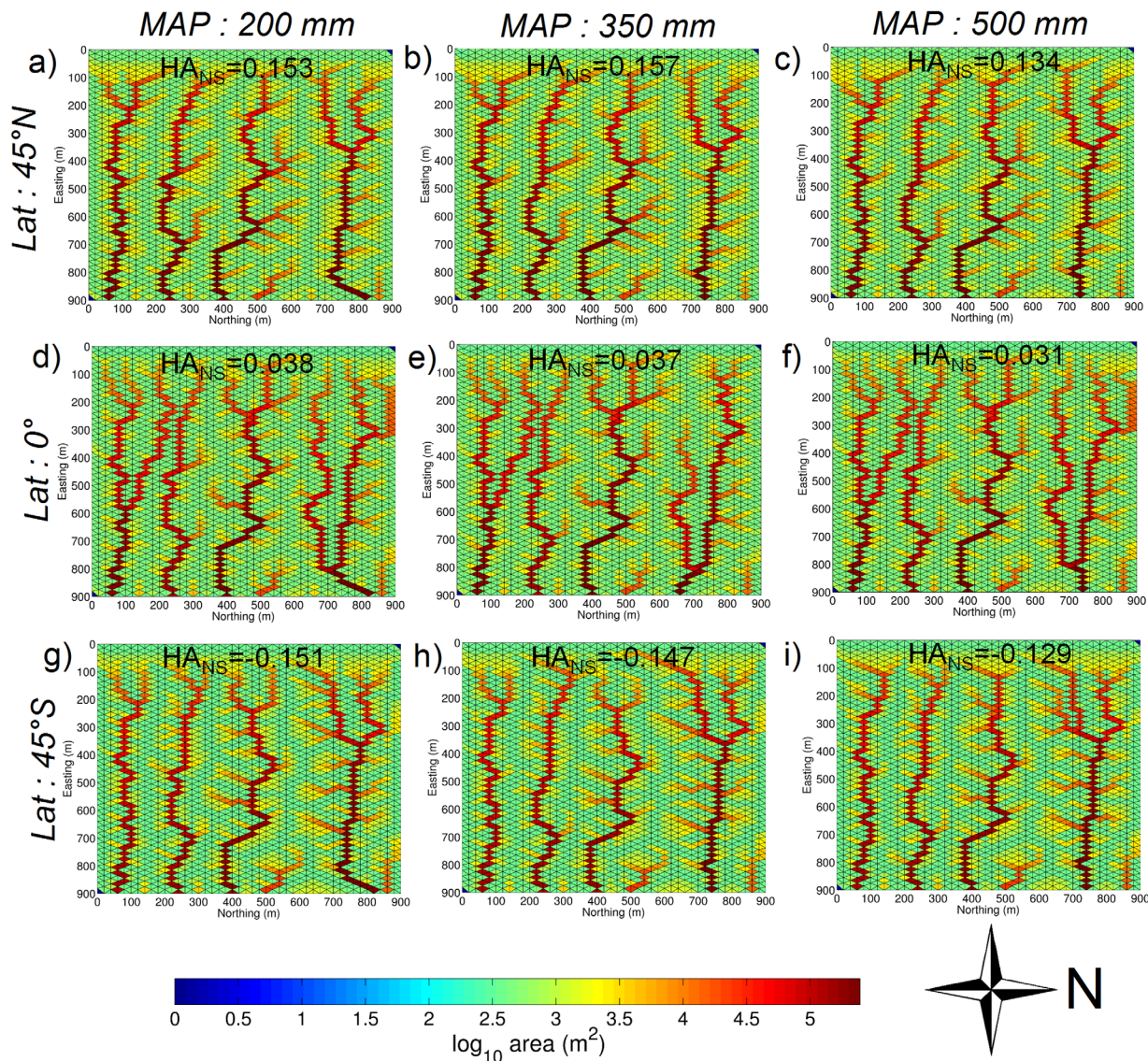


Figure 4. Upslope contributing area maps of modeled landscapes for 200, 350, and 500 mm of MAP for 45°N (a, b, c), 0° (d, e, f), and 45°S (g, h, i) latitudes. Calculated hillslope asymmetry, HA_{N-S} ($HA_{N-S} = \log_{10}[S_{North}/S_{South}]$) based on Poulos et al. [2012] for each modeled landscape is reported. The equator case is developed using northern hemisphere wet season.

on SFS by northward advance of fluvial channel heads. Enhanced fluvial processes on SFS reduce hillslope gradients, leading to a positive ($HA_{N-S} > 0.13$) landscape-scale hillslope asymmetry (Figures 4c). $HA_{N-S} = 0.15$ indicates $\sim 41\%$ steeper NFS than SFS averaged across the modeled domain. At the equator (0° latitude), channel branching is nearly symmetrical toward north and south aspects, resulting about fivefold smaller HA_{N-S} values than those reported for 45°N (Figures 4d–4f). HA_{N-S} values for s-2 scenarios of the equator case (wet season in-phase with the peak of solar radiation in the Southern Hemisphere) for MAP of 200, 350, and 500 mm are -0.020 , -0.016 , and -0.015 , respectively (not mapped in this paper). The sign change of the HA_{N-S} demonstrates the role of the timing of the wet season in the simulation results. In the Southern Hemisphere (45°S latitude), channels preferentially develop on NFS by southward channel head advance, leading to landscape asymmetry toward north ($HA_{N-S} < 0$). $|HA_{N-S}|$ for 45°S latitude are slightly lower than those at the 45°N latitude. Comparing Figures 3 and 4 clearly indicates that channels grow into aspects that receive more solar radiation within the modeled semiarid MAP range. At the equator, hillslope asymmetry is weak as R_{solar} differences between opposing NFS and SFS aspects are much less pronounced.

For a more detailed exploration of the roles of latitude and climate on hillslope asymmetry, we plot HA_{N-S} calculated from modeled landscapes from 45°N to 45°S with 15° increments as a function of latitude (Figure

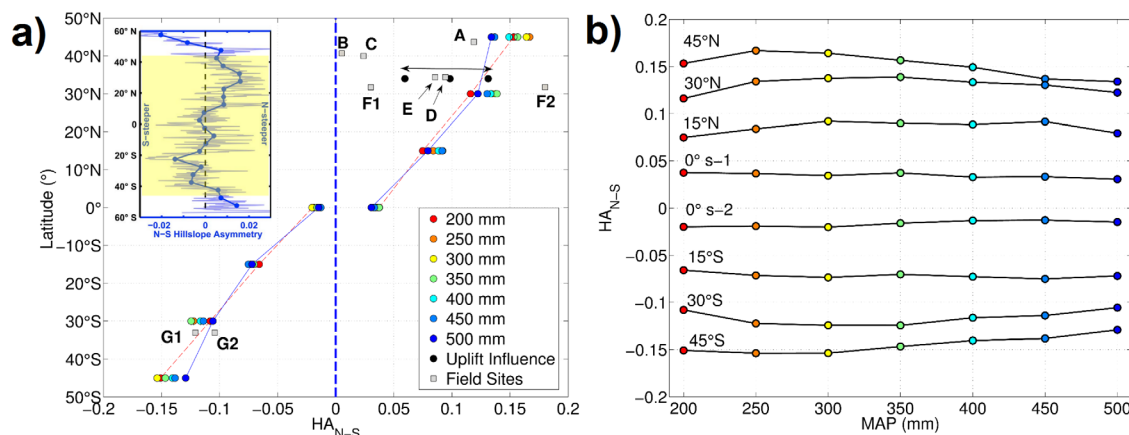


Figure 5. (a) Landscape-scale north-to-south hillslope asymmetry (H_{N-S}) plotted as a function of latitude for all: modeled landscapes with 0.1 mm/yr uplift and a range of MAP (color-coded circles); modeled landscapes with no, moderate, and high uplift for 34°N latitude for central New Mexico (black circles) with MAP = 250 mm; and some samples of observed semiarid catchments (see Table 1 for information) that exhibit aspect-related vegetation and geomorphic differences reported in the literature (gray squares). Wettest and driest MAP simulations (200 and 500 mm) are emphasized with lines connecting each modeled H_{N-S} . The inset shows the H_{N-S} through the American Cordillera calculated by Poulos *et al.* [2012] (Adapted and used from Poulos *et al.*, [2012] with permission of John Wiley and Sons). Highlighted portion in the inset shows the range of latitudes used in our model experiments. (b) H_{N-S} plotted as a function of MAP. Simulations at the equator have two different wet season timings. The s-1 and s-2 simulation scenarios correspond to wet seasons of the Northern Hemisphere and the Southern Hemisphere, respectively.

5a). The latitudinal variation of H_{N-S} values for the American Cordillera reported by Poulos *et al.* [2012] based on 90 m DEM is also given in the inset of Figure 5a [Poulos *et al.*, 2012, Figure 2] for comparison with our model results. This figure is complemented by plotting H_{N-S} as a function of MAP for each latitude to illustrate the role of wetter climate on hillslope asymmetry (Figure 5b).

Consistent with the observations of Parsons [1988] and Poulos *et al.* [2012], modeled H_{N-S} values are positive in the Northern Hemisphere and negative in the Southern Hemisphere. At a given latitude, differences in MAP manifest themselves by a range of H_{N-S} . Despite the consistency in the signs of H_{N-S} between model results and published literature that used DEMs, a close inspection of Poulos *et al.* [2012] values reveal two notable discrepancies between model results and H_{N-S} calculated across the American Cordillera (Figure 5a). First, in the modeled landscapes, H_{N-S} systematically increases (decreases) toward the poles in the Northern (Southern) Hemisphere without any discontinuity. This pattern is consistent with Poulos *et al.* [2012] only within the low-to-midlatitudes. H_{N-S} attains maximum absolute values in ~30°N and ~20°S in their data, and then begins to decrease in the Northern (increase in the Southern) Hemisphere, and finally changes sign from positive to negative above ~49°N, and from negative to positive around ~40°S. Second, modeled H_{N-S} values at the landscape scale are nearly an order of magnitude greater than those reported by Poulos *et al.* [2012]. It may be argued that the reversal in the H_{N-S} at high latitudes is due to a change in the dominant form of geomorphic processes from fluvial incisions and landsliding to periglacial and glacial processes, and changes in low to high-biomass plant species [Poulos *et al.*, 2012]. Figure 5b shows a second-order impact of MAP on H_{N-S} mostly in midlatitudes in the modeled landscapes. Evidence for a relatively small increase in absolute values of H_{N-S} can be observed for intermediate values of MAP in 15°N, 30°N, 45°N, and 45°S latitudes. However, such changes are less than ~15% of the mean H_{N-S} modeled for any given latitude.

H_{N-S} reported by Poulos *et al.* [2012] were calculated (and averaged) from a 90 m DEM, using a 5 km by 5 km sliding window. This is likely the reason why their values are smaller than the modeled ranges. Next we illustrate H_{N-S} obtained from published literature that use finer resolution DEMs (Table 1) for watersheds where vegetation differences were reported on opposing hillslope aspects (Figure 5a, indicated by A, B, C, D, E, F1, F2, G1, G2). Catchments reported for the Northern Hemisphere are located above the 30°N latitude and within the semiarid climate zone of the western U.S. The purpose of this illustration is to compare how H_{N-S} at individual sites with different histories of uplift and climate (to a limited extent), and properties of bedrock, soil, and vegetation compare with H_{N-S} predicted by the model for fixed watershed properties, driven by a narrow range of MAP, and a small sample of uplift simulations. Such a comparison is useful for developing hypotheses about the potential causes for the differences between observed and modeled H_{N-S} for future research.

Table 1. Location of Analyzed Catchments, Their DEM Resolution and Calculated HA_{N-S} Values, and Source of the Studies That Indicates Aspect-Related Vegetation Difference

Location	Latitude (°)	Longitude (°)	Elevation Range (m)	MAP (mm)	HA_{N-S}	DEM Res. (m)	Source
A ^a	N 43.72	W 116.13	1032–2125	330–890 ^b	0.119	10	<i>Poulos et al.</i> [2012]
B	N 40.69	W 105.51	2143–2334	415	0.005	10	<i>Ranney et al.</i> [2015]
C	N 40.01	W 105.47	2435–2734	519	0.024	1	<i>Anderson et al.</i> [2013b]
D	N 34.42	W 107.80	1985–2881	220–325 ^b	0.094	30	<i>Yetemen et al.</i> [2010]
E	N 34.41	W 106.98	1567–1711	250	0.086	10	<i>Istanbulluoglu et al.</i> [2008]
F1	N 31.72	W 110.03	1219–1927	312	0.030	10	Visual inspection on Google Earth
F2	N 31.74	W 109.94	1494–1576	341	0.180	10	<i>Flores Cervantes et al.</i> [2014]
G1	S 33.05	W 70.92	607–1035	593	−0.121	30	<i>Parsons</i> [1976]
G2	S 33.05	W 70.92	620–1007	593	−0.104	30	<i>Parsons</i> [1976]

^aA: Dry Creek Experimental Watershed, Boise, Idaho; B: Cache la Poudre Basin, Colorado; C: Gordon Gulch Boulder Creek Critical Zone Observatory, Boulder, Colorado; D: Upper Rio Salado, New Mexico; E: Sevilleta Long Term Ecological Research Park, New Mexico; F1: Walnut Gulch Experimental Watershed, Arizona; F2: Kendall Site in WGEW, Arizona; G1 and G2: Cerro Robles, Chile.

^bMAP is reported in a range in catchments where elevation range is high.

Since our model was initially developed and confirmed against geomorphic and ecohydrologic observations in a central New Mexico catchment (34°N latitude, MAP = 250 mm) [Yetemen et al., 2015], observations from this region can be used for model confirmation. Uplift in central New Mexico is uncertain and may vary spatially. To provide more context for the role of uplift on HA_{N-S} , additional model simulations are conducted for no uplift, intermediate (0.05 mm/yr), and high (0.1 mm/yr) uplift cases consistent with reported ranges of uplift rates for central New Mexico [e.g., Dethier et al., 1988; Pazzaglia and Hawley, 2004]. These uplift rates produced landscape-scale HA_{N-S} values of 0.060, 0.098, and 0.131, respectively (filled black circles in Figure 4a), the range of which is shown with a double-headed arrow in Figure 4a. A twofold increase in uplift produces approximately a twofold increase in HA_{N-S} , which captures a significant portion of the variability in HA_{N-S} of the sample catchments plotted in the Northern Hemisphere. For the central New Mexico catchment (34°N latitude) where our model was initially tested [Yetemen et al., 2015], HA_{N-S} is calculated as 0.086 using a 10 m DEM (labeled E in Figure 4a). The Upper Rio Salado Basin (area 465 km²) in the same region has a HA_{N-S} of 0.094, calculated from a regional 30 m DEM (labeled D in Figure 4a). Both D and E are clearly within the ranges of HA_{N-S} predicted by the LEM.

In addition to these local comparisons, we also calculated HA_{N-S} values for several semiarid catchments that show distinct aspect-controlled vegetation differences as reported in the ecological literature in the Northern Hemisphere (A, B, C, F1, and F2) and the Southern Hemisphere (G1, G2) (Table 1). The Dry Creek Experimental Watershed (DCEW), Boise, Idaho (A in Figure 4a) has HA_{N-S} slightly lower than model predictions for MAP = 500 mm (wettest simulation). MAP in Dry Creek is 560 mm (slightly wetter than our wettest model run), ranging from 370 mm (1100 m ASL) to 890 mm (1900 m ASL) with elevation [Kunkel et al., 2011], with a significant seasonal snow component [Smith et al., 2011]. The slightly lower value of the observed HA_{N-S} value in Dry Creek than those obtained from model predictions may be attributed to overall wetter conditions, and perhaps the role of snow accumulation and melt dynamics, as with increased MAP above 250 mm, modeled HA_{N-S} decreased at the 45°N latitude (Figure 4a). The two catchments in the Southern Hemisphere located in Cerro Robles, Chile fall within the range of model predictions. These catchments have broad-leaved evergreen shrubs (known as matorral in Chile) and MAP of 593 mm [Parsons, 1976].

HA_{N-S} values obtained from three other semiarid basins in the Northern Hemisphere (B, C, and F1 in Figure 4a) do not agree well with the model. Deviations from model predictions at each site however can facilitate development of testable hypothesis to address the underlying causes of their mismatch. C is the Gordon Gulch site of the Boulder Creek Critical Zone Observatory (CZO), an alpine basin (Area = 2.66 km², Mean Elevation = 2616 m with a range of 2434 m–2734 m) that has historically experienced seasonal temperature variations to below freezing conditions leading to periglacial processes including seasonal soil frost during which frost-related weathering and transport processes dominate hillslope sediment loss [Dethier and Lazarus, 2006; Leopold et al., 2013]. In colder NFS of this region, more frequent frost heave action could have led to the development of deeper weathered rock zones and more effective sediment transport than SFS, as illustrated in a recent numerical modeling study [Anderson et al., 2013a]. It can be hypothesized that periglacial processes that enhance sediment transport on NFS at this site lessen the erosion differential caused by vegetation-inhibited runoff erosion on NFS, thereby reducing the watershed-scale HA_{N-S} . To further test this

hypothesis, we plot HA_{N-S} of another high-elevation site (B in Figure 4a), the Cache La Poudre catchment near Rustic, Colorado, located about 80 km north of Gordon Gulch, and about 35 km northeast of the Pleistocene glacier in the Cache La Poudre River valley [Madole *et al.*, 1998; Benson *et al.*, 2004; Madole, 2012]. The Cache La Poudre has an area of 0.19 km², mean elevation of 2,234 m, and MAP of 415 mm [Ranney *et al.*, 2015]. Vegetation is coniferous forest with sparse deciduous shrub understory on NFS, and shrubland with sparse coniferous trees on SFS. Despite the semiarid climate and differential vegetation development on opposing NFS and SFS, near symmetrical HA_{N-S} values provide further evidence that support how enhanced weathering and sediment transport driven by periglacial processes on NFS may override the influence of vegetation causing differential erosion and hillslope asymmetry.

F1 is the Walnut Gulch Experimental Watershed (WGEW), Tombstone, AZ located at the Basin and Range Province with an area of 156.6 km² and elevation range from 1219 m to 1927 m. This site is located farther south of the maximum extent of the Pleistocene ice sheets which terminated around the northeast of the state of Kansas [e.g., Aber, 1991; Aber and Apolzer, 2004]. Moreover, the elevation range of the WGEW, 1219–1927 m, is significantly lower than the elevation of the glacier activities (higher than 3000 m) found at the peak of San Francisco Mountain in Arizona [Atwood, 1905] and the Sangre de Cristo Mountains in New Mexico [Armour *et al.*, 2002]. Therefore the role of freeze-thaw processes on weathering and landscape evolution should be negligible. This watershed has a relatively complex topographic structure dominated by alluvial fan deposits and a complex history of tectonism in the south and southeastern basin. Complex geologic and geomorphic conditions evolved by episodic faulting that began in Precambrian are poorly understood [Osterkamp, 2008]. Despite its semiarid climate, complex geology at this site could have muted the differential development of fluvial processes on opposing slopes that lead to hillslope asymmetry.

The figure also includes the HA_{N-S} of the Kendall catchment (~ 1.86 km²) located in the headwaters of the WGEW (F2), a grassland ecosystem underlain by alluvial fan deposits where semiarid climate (MAP = 341 mm, Elevation = 1526 m) supports more productive vegetation cover on NFS than SFS [Flores Cervantes *et al.*, 2014]. Dendritic channel network with distinct ridges, unchanneled valleys, and channels are characteristics of the geomorphology of the Kendall catchment, which bears the highest HA_{N-S} on the plot ($HA_{N-S} = 0.18$). Among the sites employed here to evaluate model results, the geology, climate, and vegetation conditions at the Kendall site is most closely resemble those in central New Mexico, which was initially used in the design of our model. The higher HA_{N-S} calculated for the Kendall catchment using a 10 m DEM compared to model predictions than those obtained from model simulations (as well as the HA_{N-S} of the WGEW) may thus be largely attributed to model sensitivity to parameter space.

Our results show slightly greater simulated absolute values of HA_{N-S} ($|HA_{N-S}|$) in the Northern Hemisphere than in the Southern Hemisphere (with one exception: 45° with 450 mm of MAP), but with consistent latitudinal patterns for each hemisphere. The hemispheric differences are also evident in the two sets of equatorial runs, done with different seasonality, s-1 and s-2. In the model simulations for a given degree of latitude, transpiration forcing T_{max}^F is deterministic and identical on both hemispheres but with a 6 month shift in its seasonal behavior. Rainfall forcing is also shifted by 6 months but is stochastic. The subtle hemispheric differences in $|HA_{N-S}|$ may be attributed to the stochastic nature of rainfall; all four northern latitude runs (s-1) having the same MAP used a common set of precipitation inputs, but the southern latitude runs (s-2) having the same MAP used a second set, different only in the stochastic generation. This attribution is supported by a test of model sensitivity (not shown) to initial topographic surface (landscape originally evolved) and stochastic rainfall. The test showed for a given latitude as much as 15% variability in HA_{N-S} around its mean value. This variation is small compared to the consistent latitudinal differences observed for both hemispheres in this study. The subtle differences in $|HA_{N-S}|$ between hemispheres do not in any way undermine our conclusions concerning the variations in $|HA_{N-S}|$ across latitudes.

Theoretically, an increase in $|HA_{N-S}|$ with latitude should result from a growing contrast between the steepness of opposing hillslope gradients. To illustrate and examine this behavior, spatial means of local slopes for NFS (Figure 6a) and SFS (Figure 6b) of modeled landscapes are plotted with respect to MAP for latitudes from 45°N to 45°S with 15° increments. The Figures 6a and 6b clearly show why $|HA_{N-S}|$ is positively related to latitude. Opposing NFS and SFS show the smallest difference in the modeled topography at the 0° latitude. As latitude increases northward (southward) from the equator, NFS get steeper (gentler) while SFS get gentler (steeper) compared to their corresponding values at the 0° latitude. Modeled topography for the 45°N latitude bears the shallowest SFS and the steepest NFS, while on the contrary, the steepest SFS and

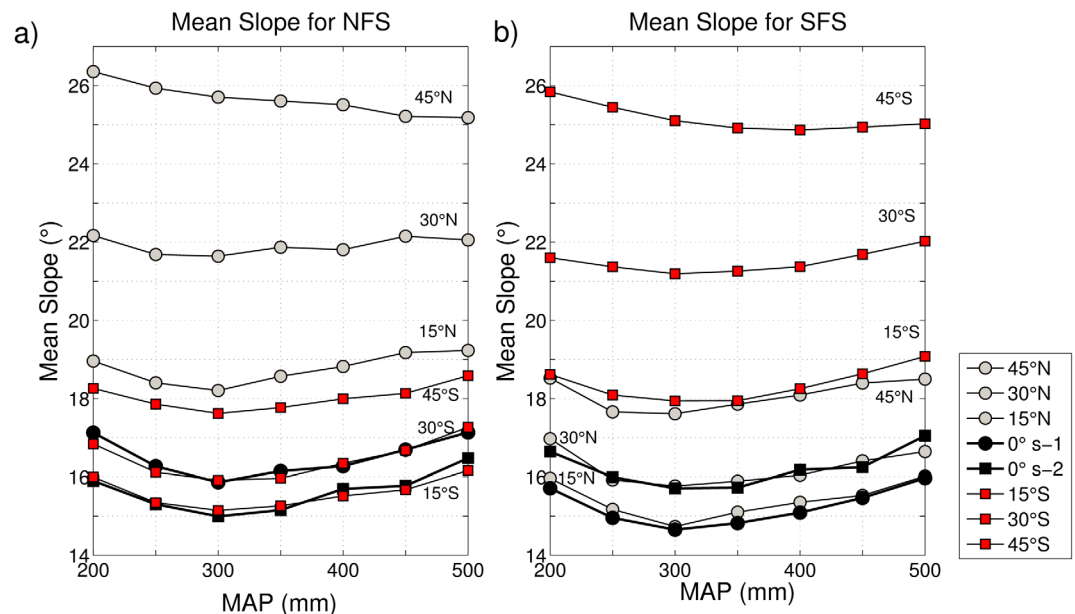


Figure 6. (a) Latitudinal variations of spatial mean slopes of modeled landscapes plotted as a function of MAP for north-facing slopes, NFS (a), and south-facing slope, SFS (b). To facilitate cross comparison of data for NFS and SFS of a model output for a given latitude, latitudes in the northern and southern hemisphere are represented with gray circles and red squares, respectively; black circles (s-1) and black squares (s-2) represent data from the equator simulated with wet season timing of the Northern Hemisphere and Southern Hemisphere, respectively.

the shallowest NFS are predicted for the 45°S latitude. Interestingly, mean slopes of NFS in modeled southern latitudes (Figure 6a) and mean slopes of SFS in modeled northern latitudes (Figure 6b) first get shallower as MAP increases from 200 mm to 300 mm, and then get steeper as climate becomes wetter. Such behavior is not as clear on the corresponding opposite aspects. This may provide an explanation to the observed slight decrease (increase) in HA_{N-S} with MAP > 300 mm in the northern (southern) latitudes (Figure 5b). With this evidence, and known limitations of our model we ask the following question: What is the mechanism by which solar radiation influences modeled landscape evolution such that the difference between the opposing NFS and SFS enhances with latitude, and, for a given latitude, slopes show a complex response to MAP? We address these questions in the next section.

4.2. Latitudinal Variations and Ecogeomorphic Interactions

In our model, vegetation-fluvial incision/transport interactions are the only built-in mechanisms by which slopes evolve differentially as a function of latitude. Therefore quantifying how vegetation responds to latitude and climate on opposing aspects will give direct evidence for the role of aspect on fluvial landscape evolution. To examine the vegetation response to aspect in both the Northern Hemisphere and the Southern Hemisphere, we use the last 100 years of vegetation cover fraction (V_t) outputs at each model element (model grid cell) at a temporal resolution of interstorm duration. We calculate the 100 year average of V_t at each model element ($\overline{V_t}$), group the $\overline{V_t}$ data into separate bins for NFS and SFS, and plot each bin data using Box-Whisker plots for 0°, 15°, 30°, and 45° latitude simulations for both hemispheres, for MAP of 200, 350, and 500 mm (Figures 7a and 7b). The $\overline{V_t}$ values for s-1 and s-2 scenarios for 0° latitude are shown in Figure 7a and 7b, respectively. To facilitate comparison between NFS and SFS for a given MAP, model outputs for opposing slopes are plotted with some distance between them to avoid overlapping. The observed range in the whiskers shows the spatial variability of $\overline{V_t}$ for each aspect. $\overline{V_t}$ values are naturally low as they reflect the average of growing (rainy) and nongrowing seasons. $\overline{V_t}$ on each aspect increase in the direction of increase in MAP as indicated in the figure legend.

A clear separation between NFS and SFS can be observed for each MAP plotted, where NFS sustain overall higher and more variable V_t than SFS as latitude grows (Figure 7a). At the 0° latitude, V_t values on NFS and SFS for s-1 and s-2 scenarios are nearly identical and show very small spatial variability while V_t mainly increases with MAP (Figures 7a and 7b). This can be directly related to the relatively lower range of seasonal

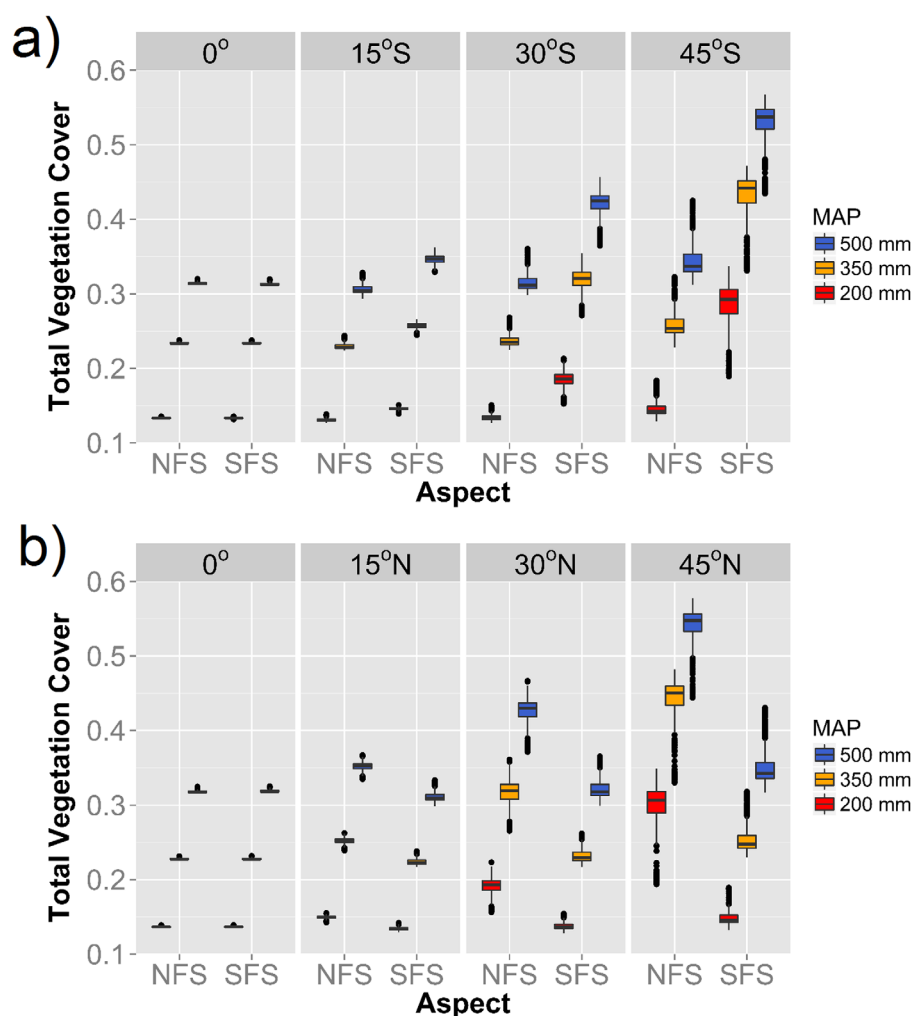


Figure 7. Mean annual total vegetation cover V_t at north and south-facing slopes for the last 100 year of the simulations at different latitudes (0° , 15° , 30° , and 45°) for the Northern Hemisphere (a) and the Southern Hemisphere (b) are shown in Box-Whisker plots as a function of MAP. Note that, the 0° latitude simulations are forced with wet season timing of the Northern Hemisphere (a) (s-1 scenario) and the Southern Hemisphere (b) (s-2 scenario). Each boxplot, the box corresponds to the interquartile range defined by lower and upper quartiles, the line in box corresponds to the median value and the whiskers to either the maximum or minimum value of V_t . Dots represent the outlier values which are 1.5 times of the interquartile range greater than the value of the upper quartile or 1.5 times of the interquartile range smaller than the value of the lower quartile.

contrast in the spatial distribution of solar radiation on both NFS and SFS at the 0° latitude (Figures 3e and 3f). At higher northern latitudes, growing contrast in the spatial distribution of solar radiation leads to more (less) solar radiation on SFS (NFS) especially during the fall and winter months (Figures 3a and 3b). Solar radiation remains slightly elevated on SFS during the growing season. Such differences reduce V_t on SFS and enhance V_t on NFS compared to V_t at the 0° latitude. Loss of V_t on SFS in the Northern Hemisphere has been related to greater soil moisture depletion as a result of higher demand for ET during the fall and winter months, leading to drier initial conditions of soil moisture for the growing season than soil moisture on NFS [Gutiérrez-Jurado and Vivoni, 2013a, 2013b; Yetemen et al., 2015]. Relatively drier soils combined with slightly higher solar radiation exposure during the growing season amplify plant water stress, making SFS less advantageous than NFS for vegetation growth [Yetemen et al., 2015]. In addition, drier and warmer conditions in SFS were predicted to cause much rapid grass senescence [Zhou et al., 2013; Yetemen et al., 2015]. These model responses are supported by ecohydrologic field observations on opposing NFS and SFS in central New Mexico [Gutiérrez-Jurado et al., 2013]. It is also interesting to note that even though R_{solar} increases on SFS toward higher latitudes in the Northern Hemisphere, a concomitant reduction in annual R_{cs} and increase in its seasonal variability (Figure 1) results a slight increase of V_t and its year-to-year variability on

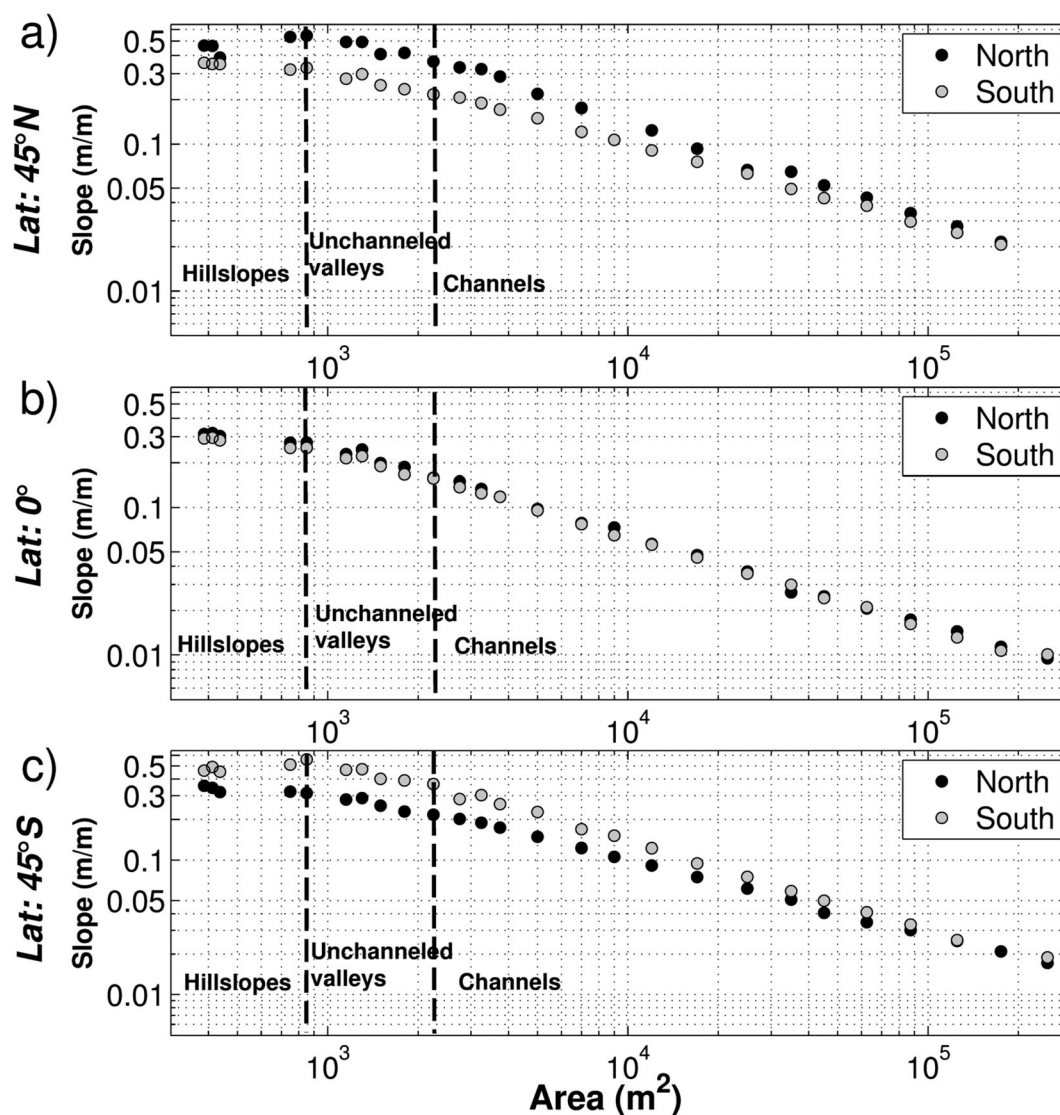


Figure 8. The slope-area relation of modeled landscapes with a MAP = 350 mm for (a) 45°N, (b) 0°, and (c) 45°S latitudes. Each data point presents an average slope of binned model elements with respect to area. The 0° latitude simulation represents the model run with the wet season timing of the northern hemisphere (s-1 scenario).

SFS especially for latitudes greater than 15°N. In the Southern Hemisphere, modeled patterns described above are reversed. SFS hold denser canopy cover than NFS as they receive less solar radiation.

On an evolving modeled topography, emerging vegetation differences on opposing slopes create a feedback mechanism with fluvial erosion and transport rules in the model leading to differential landscape evolution with respect to aspect. The relationship between local slope and upslope contributing area (S-A) can be used to quantitatively illustrate the role of latitude on catchment organization. The S-A data for 45°N, 0° (for s-1 scenario), and 45°S simulations driven by MAP = 350 mm are presented in Figure 8. On a S-A plot, convex hillslopes exhibit a positive S-A relation, illustrated by the first vertical dashed line in Figure 8, while concave valleys and channels exhibit a negative S-A relation [e.g., Tucker and Bras, 1998]. The second vertical-dashed line designates the beginning of fluvial channels (to the right of the line), extracted based on cumulative distribution of drainage areas [e.g., Ijjasz-Vasquez and Bras, 1995; Yetemen et al., 2010]. Unchanneled valleys are technically located between the two vertical dashed lines, with greater convexity in the S-A relation that erode by a mixture of hillslope diffusion and less frequent fluvial processes [Istanbul-luoglu et al., 2008]. In Figure 8a, the mean slope values of NFS are greater than those of SFS ($p < 0.0001$). In the Southern Hemisphere, the mean slope values of SFS are greater than those of NFS ($p < 0.0001$) (Figure

8c). In channels where slopes decay with area, differences between NFS and SFS drop. This figure provides another direct evidence for hillslope asymmetry largely pronounced at the scale of hillslope and unchanneled valleys, where local slopes are steeper than channels.

Evolution of the landscape S-A relation can be explained in relation to catchment ecohydrologic dynamics. Vegetation cover reduces the effective shear stress used for fluvial incision and transport (Figure 2g). Therefore, in an equilibrium landscape on northern latitudes under constant regional uplift, NFS that are more resistive to fluvial erosion as a result of denser grass cover (Figure 7a) tend to get steeper (Figure 8a), promoting transport by soil creep to compensate the loss of fluvial transport by hillslope diffusion, and hence maintain the uplift-erosion balance. In contrast, more erodible SFS in the Northern Hemisphere can maintain the uplift-erosion balance by adjusting to gentler slopes than their NFS counterparts (Figure 7a) as fluvial transport depends on both discharge and local slope, and fluvial transport is more effective in removing sediments than hillslope diffusion. As solar radiation exposure reverses between NFS and SFS in the Southern Hemisphere, the abovementioned radiation-driven coupled ecogeomorphic processes lead to denser vegetation cover and steeper hillslope gradients on SFS than NFS, resulting in $HA_{N-S} < 0$ (Figure 8c). Consistent with the theory, the relatively low radiation contrast at the 0° latitude does not prompt any significant differences in the S-A relations for the equator case (Figure 8b).

5. Conclusions

In this study, we used the CHILD ecogeomorphic landscape evolution model (LEM) that couples the continuity equations for water, sediment, and aboveground biomass, driven by constant uplift, stochastic rainfall, and solar radiation distributed in space and time. Modeled geomorphic transport phenomenon was limited to fluvial and diffusive flux rules. The influence of latitude on hillslope asymmetry from 45°S to 45°N is explored for semiarid climate and ecosystem conditions. A hillslope asymmetry index defined as the log of ratio of median slopes of north-facing slopes (NFS) and south-facing slopes (HA_{N-S}), and the slope—area plot (for select simulations) are used to discuss findings. The main conclusions are:

1. As landscape slopes form in the Northern Hemisphere, SFS receive greater insolation than NFS, and therefore become more water stressed, developing sparser vegetation cover than NFS. Surface runoff flowing on sparser vegetation cover more effectively erode sediments and further disrupt vegetation. In contrast, denser vegetation on NFS reduces fluvial erosion efficiency. As the landscape evolves to uplift-erosion equilibrium, less insulated NFS thus get steeper than more insulated SFS to compensate for their lower fluvial transport efficiency. The controlling processes are identical in the Southern Hemisphere, but the orientation is reversed, with SFS receiving less insolation develop steeper slopes while NFS receiving more insolation develop shallower slopes. Thus, in summary, in fluvially eroding vegetated landscapes, the slopes facing the poles get steeper than those facing the equator to compensate for their lower transport efficiency induced by denser vegetation cover.
2. The model results show that HA_{N-S} is a direct outcome of differences in solar radiation-driven vegetation productivity, an effect that is magnified at high latitudes. In the model, less insulated (pole-ward) slopes support more vegetation cover than more insulated (equator-ward) slopes. The vegetation contrast increases with latitude, with the primary changes on the poleward slopes. In the Northern Hemisphere, modeled HA_{N-S} is positive and linearly increases with latitude. Predicted HA_{N-S} was found within the range of those calculated for actual fluvial landscapes with contrasting vegetation productivity on opposing aspects in the Northern Hemisphere, however, are higher than catchments experienced glacial and periglacial surface processes. This differences is hypothesized to be related to the influence of glacial and periglacial processes. In the Southern Hemisphere, modeled HA_{N-S} is negative and linearly decreases with latitude.
3. Compared with the primary effect of solar insolation, which varies strongly with latitude, MAP exerts only a secondary control on hillslope asymmetry. The role of MAP on hillslope asymmetry is most pronounced at mid and high latitudes, where reduced annual solar radiation and growing contrast in the spatial distribution of solar radiation on opposing aspect enhances HA_{N-S} through vegetation feedback.

While the model provided new insights into hillslope asymmetry, it has several limitations. In the model, the coupling between ecohydrology and geomorphology is limited to fluvial processes.

There is growing evidence that aspect-modulated microclimate can also influence colluvial transport by hillslope diffusion [West *et al.*, 2014] and the rates of bedrock weathering [Burnett *et al.*, 2008]. Observed hillslope asymmetry from catchments at high elevations shows that glacial and periglacial processes can be effective on hillslope asymmetry, which are not included in the model. Our model operates with a single vegetation type and constant climate. Glacial and interglacial cycles and accompanying changes in vegetation type remain to be a critical limitation. Future efforts should be directed at incorporating the effects of hillslope diffusion, glacial, and periglacial processes on hillslope asymmetry with the integration of multiple plant types in modeled landscapes under cyclic climate.

Acknowledgments

Simulation results can be obtained from the first author on request. The DEM data cited in this manuscript are publicly available and can be accessed from the following repositories: 1-arc DEM data (~30 m) for Upper Rio Salado and Cerro Robles and 10 m DEM data for Cache La Poudre are available at online repository of USGS National Elevation Data set (<http://nationalmap.gov/elevation.html>) and SRTM 1 arc-second Global Data set (<http://earthexplorer.usgs.gov/>), respectively. 1 m LiDAR data for Gordon Gulch are available at Boulder Creek CZO online data repository (<http://czo.colorado.edu/geGIS/geGIS.shtml>). 10 m DEM data for Dry Creek are available at Dry Creek Experimental Watershed online data repository (<http://earth.boisestate.edu/drycreek/data/spatial-data/>). 10 m DEM data for Walnut Gulch are available at Southwest Watershed Research Center's online data repository (<http://www.tucson.ars.ag.gov/dap/>). 10 m DEM data for Sevilleta are available at Sevilleta LTER online repository (<http://sev.lternet.edu/>). We thank Patricia Saco (AE), Daniel B. Collins, and two anonymous reviewers for their comments, which contributed to improving this paper. We thank Alan G. Barr (Environment Canada) for his helpful comments on the manuscript, Zilefac Asong and Willemijn Appels (both from the University of Saskatchewan) for their help for figure preparations. Simulations are run at different clusters. We acknowledge support from the Research Computing Group of the University of Saskatchewan for using the cluster Plato; the GIWS at the University of Saskatchewan for using cluster Water, and the University of Colorado—CSDMS for using the cluster Beach. We thank NSF for financial support provided through grants: NSF-EAR 0963858, NSF-ACI 1148305. Yetemen acknowledges support from the GSA Farouk El-Baz student research award.

References

- Aber, J. S. (1991), The glaciation of northeastern Kansas, *Boreas*, 20(4), 297–314, doi:10.1111/j.1502-3885.1991.tb00282.x.
- Aber, J. S., and K. Apolzer (2004), Pre-Wisconsinan glacial database and ice limits in the central United States, in *Developments in Quaternary Sciences*, edited by J. Ehlers and P. L. Gibbard, pp. 83–88, Elsevier, Amsterdam, Netherlands.
- Allen, R. G., L. S. Pereira, D. Raes, and M. Smith (1998), Crop evapotranspiration: Guidelines for computing crop water requirements, *FAO Irrig. Drain. Pap.*, 56, Food and Agric. Organ. of the U. N., Rome, Italy.
- Almond, P. C., J. J. Roering, M. W. Hughes, F. S. Lutter, and C. Leblouteiller (2008), Climatic and anthropogenic effects on soil transport rates and hillslope evolution, Sediment Dynamics in Changing Environments, Christchurch, New Zealand, *IAHS Publ.*, 325, 417–424.
- Anderson, R. S., S. P. Anderson, and G. E. Tucker (2013a), Rock damage and regolith transport by frost: An example of climate modulation of the geomorphology of the critical zone, *Earth Surf. Processes Landforms*, 38(3), 299–316, doi:10.1002/esp.3330.
- Anderson, S. P., R. S. Anderson, G. E. Tucker, and D. P. Dethier (2013b), Critical zone evolution: Climate and exhumation in the Colorado Front Range, *Field Guides*, 33, 1–18, doi:10.1130/2013.0033(01).
- Armour, J., P. J. Fawcett, and J. W. Geissman (2002), 15 k.y. paleoclimatic and glacial record from northern New Mexico, *Geology*, 30(8), 723–726, doi:10.1130/0091-7613(2002)030<0723:KYPAGR>2.0.CO;2.
- Atwood, W. W. (1905), Glaciation of San Francisco Mountain, Arizona, *J. Geol.*, 13(3), 276–279, doi:10.2307/30067938.
- Benson, L., R. Madole, W. Phillips, G. Landis, T. Thomas, and P. Kubik (2004), The probable importance of snow and sediment shielding on cosmogenic ages of north-central Colorado Pinedale and pre-Pinedale moraines, *Quaternary Sci. Rev.*, 23(1–2), 193–206, doi:10.1016/j.quascirev.2003.07.002.
- Black, T. A., and D. R. Montgomery (1991), Sediment transport by burrowing mammals, Marin County, California, *Earth Surf. Process. Landforms*, 16(2), 163–172, doi:10.1002/esp.3290160207.
- Branson, F. A., and L. M. Shown (1989), *Contrasts of Vegetation, Soils, Microclimates, and Geomorphic Processes Between North- and South-Facing Slopes on Green Mountain Near Denver, Colorado*, Dept. of the Int., U.S. Geol. Surv., Denver, Colo.
- Bras, R. L. (1990), *Hydrology: An Introduction to Hydrologic Science*, pp. 19–51, Addison-Wesley, Reading, Mass.
- Burnett, B. N., G. A. Meyer, and L. D. McFadden (2008), Aspect-related microclimatic influences on slope forms and processes, northeastern Arizona, *J. Geophys. Res.*, 113, F03002, doi:10.1029/2007JF000789.
- Carson, M. A., and M. J. Kirkby (1972), *Hillslope Form and Process*, Cambridge Univ. Press, Cambridge, U. K.
- Collins, D. B. G., and R. L. Bras (2010), Climatic and ecological controls of equilibrium drainage density, relief, and channel concavity in dry lands, *Water Resour. Res.*, 46, W04508, doi:10.1029/2009WR008615.
- Collins, D. B. G., R. L. Bras, and G. E. Tucker (2004), Modeling the effects of vegetation-erosion coupling on landscape evolution, *J. Geophys. Res.*, 109, F03004, doi:10.1029/2003JF000028.
- Cristea, N. C., S. K. Kampf, and S. J. Burges (2013), Linear models for estimating annual and growing season reference evapotranspiration using averages of weather variables, *Int. J. Climatol.*, 33(2), 376–387, doi:10.1002/joc.3430.
- Dethier, D. P., and E. D. Lazarus (2006), Geomorphic inferences from regolith thickness, chemical denudation and CRN erosion rates near the glacial limit, Boulder Creek catchment and vicinity, Colorado, *Geomorphology*, 75(3–4), 384–399, doi:10.1016/j.geomorph.2005.07.029.
- Dethier, D. P., C. D. Harrington, and M. J. Aldrich (1988), Late Cenozoic rates of erosion in the western Española basin, New Mexico: Evidence from geologic dating of erosion surfaces, *Bull. Geol. Soc. Am.*, 100(6), 928–937, doi:10.1130/0016-7606(1988)100<0928:LCROEI>2.3.CO;2.
- Dingman, S. L. (2002), *Physical Hydrology*, 2nd ed., pp. 601–607, Prentice Hall, Upper Saddle River, N. J.
- Flores-Cervantes, J. H. (2010), The coupled development of terrain and vegetation: The case of semiarid grasslands, PhD thesis, MIT Press, Boston, Mass.
- Flores Cervantes, J. H., E. Istanbuluoglu, E. R. Vivoni, C. D. Holifield Collins, and R. L. Bras (2014), A geomorphic perspective on terrain-modulated organization of vegetation productivity: Analysis in two semiarid grassland ecosystems in Southwestern United States, *Ecohydrology*, 7(2), 242–257, doi:10.1002/eco.1333.
- Gabet, E. J. (2003), Sediment transport by dry ravel, *J. Geophys. Res.*, 108(B1), 2049, doi:10.1029/2001JB001686.
- Gutiérrez-Jurado, H. A., and E. R. Vivoni (2013a), Ecogeomorphic expressions of an aspect-controlled semiarid basin: I. Topographic analyses with high-resolution data sets, *Ecohydrology*, 6(1), 8–23, doi:10.1002/eco.280.
- Gutiérrez-Jurado, H. A., and E. R. Vivoni (2013b), Ecogeomorphic expressions of an aspect-controlled semiarid basin: II. Topographic and vegetation controls on solar irradiance, *Ecohydrology*, 6(1), 24–37, doi:10.1002/eco.1263.
- Gutiérrez-Jurado, H. A., E. R. Vivoni, C. Cikosi, J. B. J. Harrison, R. L. Bras, and E. Istanbuluoglu (2013), On the observed ecohydrologic dynamics of a semiarid basin with aspect-delimited ecosystems, *Water Resour. Res.*, 49, 8263–8284, doi:10.1002/2013WR014364.
- Hadley, R. F. (1961), Some effects of microclimate on slope morphology and drainage basin development, in *Geological Survey Research 1961*, edited by Department of the Interior United States Geological Survey, pp. B32–B34, Gov. Print. Off., Washington, D. C.
- Hanks, T. C. (2000), The age of scarp-like landforms from diffusion-equation analysis, in *Quaternary Geochronology: Methods and Applications*, vol. 4, edited by J. S. Noller, J. M. Sowers, and W. R. Lettis, pp. 313–338, AGU, Washington, D. C.
- Hargreaves, G. H., and Z. A. Samani (1982), Estimating potential evapotranspiration, *J. Irrig. Drain. Div.*, 108(3), 225–230.
- Hughes, M., P. Almond, and J. J. Roering (2009), Increased sediment transport via bioturbation at the last glacial-interglacial transition, *Geology*, 37, 919–922, doi:10.1130/G30159A.1.

- Ijjasz-Vasquez, E. J., and R. L. Bras (1995), Scaling regimes of local slope versus contributing area in digital elevation models, *Geomorphology*, 12(4), 299–311, doi:10.1016/0169-555X(95)00012-T.
- Istanbulluoglu, E., and R. L. Bras (2005), Vegetation-modulated landscape evolution: Effects of vegetation on landscape processes, drainage density, and topography, *J. Geophys. Res.*, 110, F02012, doi:10.1029/2004JF000249.
- Istanbulluoglu, E., and R. L. Bras (2006), On the dynamics of soil moisture, vegetation, and erosion: Implications of climate variability and change, *Water Resour. Res.*, 42, W06418, doi:10.1029/2005WR004113.
- Istanbulluoglu, E., O. Yetemen, E. R. Vivoni, H. A. Gutierrez-Jurado, and R. L. Bras (2008), Eco-geomorphic implications of hillslope aspect: Inferences from analysis of landscape morphology in central New Mexico, *Geophys. Res. Lett.*, 35, L14403, doi:10.1029/2008GL034477.
- Istanbulluoglu, E., T. J. Wang, and D. A. Wedin (2012), Evaluation of ecohydrologic model parsimony at local and regional scales in a semi-arid grassland ecosystem, *Ecohydrology*, 5(1), 121–142, doi:10.1002/eco.211.
- Ivanov, V. Y., E. R. Vivoni, R. L. Bras, and D. Entekhabi (2004), Catchment hydrologic response with a fully distributed triangulated irregular network model, *Water Resour. Res.*, 40, W11102, doi:10.1029/2004WR003218.
- Kunkel, M. L., A. N. Flores, T. J. Smith, J. P. McNamara, and S. G. Benner (2011), A simplified approach for estimating soil carbon and nitrogen stocks in semi-arid complex terrain, *Geoderma*, 165(1), 1–11, doi:10.1016/j.geoderma.2011.06.011.
- Laio, F., A. Porporato, L. Ridolfi, and I. Rodriguez-Iturbe (2001), Plants in water-controlled ecosystems: Active role in hydrologic processes and response to water stress II. Probabilistic soil moisture dynamics, *Adv. Water Resour.*, 24(7), 707–723, doi:10.1016/S0309-1708(01)00005-7.
- Leopold, M., J. Volkel, J. Huber, and D. Dethier (2013), Subsurface architecture of the Boulder Creek critical zone observatory from electrical resistivity tomography, *Earth Surf. Processes Landforms*, 38(12), 1417–1431, doi:10.1002/esp.3420.
- Ma, L., F. Chabaux, N. West, E. Kirby, L. X. Jin, and S. Brantley (2013), Regolith production and transport in the Susquehanna Shale Hills Critical Zone Observatory, Part 1: Insights from U-series isotopes, *J. Geophys. Res. Earth*, 118, 722–740, doi:10.1002/jgrf.20037.
- Madole, R. F., D. P. VanSistine, and J. A. Michael (1998), Glaciation in the Upper Platte River Drainage Basin, Colorado, *U.S. Geol. Surv. Geol. Invest. Map* 1-2644.
- Martin, Y. (2000), Modelling hillslope evolution: linear and nonlinear transport relations, *Geomorphology*, 34(1-2), 1–21, doi:10.1016/S0169-555X(99)00127-0.
- Melton, M. A. (1960), Intravalley variation in slope angles related to microclimate and erosional environment, *Bull. Geol. Soc. Am.*, 71, 133–144, doi:10.1130/0016-7606(1960)71[133:IVISAR]2.0.CO;2.
- Montaldo, N., R. Rondena, J. D. Albertson, and M. Mancini (2005), Parsimonious modeling of vegetation dynamics for ecohydrologic studies of water-limited ecosystems, *Water Resour. Res.*, 41, W10416, doi:10.1029/2005WR004094.
- Nash, D. B. (1980), Forms of bluffs degraded for different lengths of time in Emmett County, Michigan, USA, *Earth Surf. Process. Landforms*, 5, 331–345.
- Naylor, S., and E. J. Gabet (2007), Valley asymmetry and glacial versus nonglacial erosion in the Bitterroot Range, Montana, USA, *Geology*, 35(4), 375–378, doi:10.1130/G23283A.1.
- Osterkamp, W. R. (2008), Geology, soils, and geomorphology of the Walnut Gulch Experimental Watershed, Tombstone, Arizona, *J. Ariz. Nev. Acad. Sci.*, 40(2), 136–154, doi:10.2181/1533-6085-40.2.136.
- Parsons, A. J. (1988), *Hillslope Form*, Routledge, London, U. K.
- Parsons, D. J. (1976), Vegetation structure in the Mediterranean scrub communities of California and Chile, *J. Ecol.*, 64(2), 435–447, doi:10.2307/2258767.
- Pazzaglia, F. J., and J. W. Hawley (2004), Neogene (rift flank) and Quaternary geology and geomorphology, in *The Geology of New Mexico a Geologic History*, New Mexico Geol. Soc. Spec. Publ., vol. 11, edited by G. H. Mack and K. A. Giles, pp. 407–437, New Mexico Geological Society, Albuquerque, N. M.
- Pierce, K. L., and S. M. Colman (1986), Effect of height and orientation (microclimate) on geomorphic degradation rates and processes, late-glacial terrace scarps in central Idaho, *Geol. Soc. Am. Bull.*, 97(7), 869–885, doi:10.1130/0016-7606(1986)97<869:EOHAOM>2.0.CO;2.
- Poulos, M. J., J. L. Pierce, A. N. Flores, and S. G. Benner (2012), Hillslope asymmetry maps reveal widespread, multi-scale organization, *Geophys. Res. Lett.*, 39, L06406, doi:10.1029/2012GL051283.
- Ranney, K. J., J. D. Niemann, B. M. Lehman, T. R. Green, and A. S. Jones (2015), A method to downscale soil moisture to fine resolutions using topographic, vegetation, and soil data, *Adv. Water Resour.*, 76, 81–96, doi:10.1016/j.advwatres.2014.12.003.
- Rodriguez-Iturbe, I., and P. S. Eagleson (1987), Mathematical-models of rainstorm events in space and time, *Water Resour. Res.*, 23(1), 181–190, doi:10.1029/WR023i001p00181.
- Roering, J. J., J. W. Kirchner, and W. E. Dietrich (1999), Evidence for nonlinear, diffusive sediment transport on hillslopes and implications for landscape morphology, *Water Resour. Res.*, 35(3), 853–870, doi:10.1029/1998WR900090.
- Roering, J. J., P. Almond, P. Tonkin, and J. McKean (2002), Soil transport driven by biological processes over millennial time scales, *Geology*, 30(12), 1115–1118, doi:10.1130/0091-7613(2002)030<1115:Stdbrp>2.0.Co;2.
- Roering, J. J., P. Almond, P. Tonkin, and J. McKean (2004), Constraining climatic controls on hillslope dynamics using a coupled model for the transport of soil and tracers: Application to loess-mantled hillslopes, South Island, New Zealand, *J. Geophys. Res.-Earth*, 109(F1), F01010, doi:10.1029/2003JF000034.
- Small, E. E. (2005), Climatic controls on diffuse groundwater recharge in semiarid environments of the southwestern United States, *Water Resour. Res.*, 41, W04012, doi:10.1029/2004WR003193.
- Smith, T. J., J. P. McNamara, A. N. Flores, M. M. Gribb, P. S. Aishlin, and S. G. Benner (2011), Small soil storage capacity limits benefit of winter snowpack to upland vegetation, *Hydrol. Processes*, 25(25), 3858–3865, doi:10.1002/hyp.8340.
- Thornton, P. E., and S. W. Running (1999), An improved algorithm for estimating incident daily solar radiation from measurements of temperature, humidity, and precipitation, *Agric. For. Meteorol.*, 93(4), 211–228, doi:10.1016/S0168-1923(98)00126-9.
- Tucker, G. E., and R. L. Bras (1998), Hillslope processes, drainage density, and landscape morphology, *Water Resour. Res.*, 34(10), 2751–2764, doi:10.1029/98WR01474.
- Tucker, G. E., S. T. Lancaster, N. M. Gasparini, and R. L. Bras (2001), The Channel-Hillslope Integrated Landscape Development model (CHILD), in *Landscape Erosion and Evolution Modeling*, edited by R. S. Harmon and W. W. Doe III, pp. 349–388, Kluwer Acad., N. Y.
- Vivoni, E. R., H. A. Moreno, G. Mascaro, J. C. Rodriguez, C. J. Watts, J. Garatuza-Payan, and R. L. Scott (2008), Observed relation between evapotranspiration and soil moisture in the North American monsoon region, *Geophys. Res. Lett.*, 35, L22403, doi:10.1029/2008GL036001.
- Walker, E. H. (1948), Differential erosion on slopes of northern and southern exposure in western Wyoming, *Geol. Soc. Am. Bull.*, 59(12), 1360–1360.

- West, N., E. Kirby, P. Bierman, R. Slingerland, L. Ma, D. Rood, and S. Brantley (2013), Regolith production and transport at the Susquehanna Shale Hills Critical Zone Observatory, Part 2: Insights from meteoric ^{10}Be , *J. Geophys. Res. Earth*, *118*, 1877–1896, doi:10.1002/jgrf.20121.
- West, N., E. Kirby, P. Bierman, and B. A. Clarke (2014), Aspect-dependent variations in regolith creep revealed by meteoric ^{10}Be , *Geology*, *42*, 507–510, 10.1130/G35357.1.
- Williams, C. A., and J. D. Albertson (2005), Contrasting short- and long-timescale effects of vegetation dynamics on water and carbon fluxes in water-limited ecosystems, *Water Resour. Res.*, *41*, W06005, doi:10.1029/2004WR003750.
- Yetemen, O., E. Istanbuluoglu, and E. R. Vivoni (2010), The implications of geology, soils, and vegetation on landscape morphology: Inferences from semi-arid basins with complex vegetation patterns in Central New Mexico, USA, *Geomorphology*, *116*(3–4), 246–263, doi: 10.1016/j.geomorph.2009.11.026.
- Yetemen, O., E. Istanbuluoglu, J.H. Flores-Cervantes, E.R. Vivoni, and R.L. Bras (2015), Ecohydrologic role of solar radiation on landscape evolution, *Water Resour. Res.*, *51*, 1127–1157, doi:10.1002/2014WR016169.
- Zhou, X., E. Istanbuluoglu, and E. R. Vivoni (2013), Modeling the ecohydrological role of aspect-controlled radiation on tree-grass-shrub coexistence in a semiarid climate, *Water Resour. Res.*, *49*, 2872–2895, doi:10.1002/wrcr.20259.